ISIJ International, Vol. 54 (2014), No. 10, pp. 2314–2323

Measurements of Molten Steel Surface Velocity and Effect of Stopper-rod Movement on Transient Multiphase Fluid Flow in Continuous Casting

Rui LIU,[1] Brian G. THOMAS,[1]* Joydeep SENGUPTA,[2] Stephen D. CHUNG[3] and ManhKha TRINH[3]

1) Department of Mechanical Science and Engineering, University of Illinois at Urbana-Champaign, 1206 West Green Street, Urbana, IL 61801. 2) Global R&D – Hamilton, ArcelorMittal Dofasco Inc., 1390 Burlington Street East, Hamilton, Ontario L8N 3J5 Canada. 3) Steelmaking Technology, ArcelorMittal Dofasco Inc., 1330 Burlington Street East, Hamilton, Ontario L8N 3J5 Canada.

(*Received on March 30, 2014; accepted on July 3, 2014*)

Surface velocity of the molten steel in the mold is critical to final product quality during continuous casting of steel, and is one of the few flow parameters that can be measured in the plant to validate fluid flow models. Surface velocity was measured using two different sensors: Sub-meniscus Velocity Control (SVC) devices and nail dipping, to evaluate their performance, and to quantify surface velocities in a commercial steel caster under different casting speeds, argon gas fractions, and mold widths. A correlation between the height difference of the solidified lump on the nail and surface velocity is confirmed and extended. Reasonable agreement between the two sensing methods was obtained, both in trends and magnitudes for both time-averaged velocity and transient flows. Transient CFD models are applied to simulate multiphase flow of steel and gas bubbles in the Submerged Entry Nozzle (SEN) and mold and are validated with nail dipping measurements. To obtain the transient inlet boundary conditions for the simulation, two semi-empirical models, a stopper-position-based model and a metal-level-based model, predict the liquid steel flow rate through the SEN based on recorded plant data. The model system was applied to study the effects of stopper rod movements on transient flow in the SEN and mold. Mold level fluctuations were calculated using a simple pressure method and compared with plant measurements. The results show that severe stopper rod movements cause significant disturbances of the meniscus level, which may cause slag entrapment, leading to sliver defects in the final product.

KEY WORDS: steel surface velocity measurement; nail dipping; Sub-meniscus Velocity Control (SVC); continuous casting; transient multi-phase CFD model; stopper-rod movement.

1. Introduction

Many defects in steel products are caused by entrainment and entrapment of slag droplets and inclusion particles into the solidifying shell during continuous casting (CC) of steel (**Fig. 1**(a)), which is directly related to fluid flow in the mold region. Many different mechanisms for slag entrainment have been proposed and investigated in past decades,[1,2] which were recently reviewed and summarized into 9 categories.[3] These mechanisms include: mold level fluctuations, shear instability at the slag/steel interface; and are influenced by argon gas bubbles.[1] Flow-related problems at the meniscus can also cause surface defects.[4] Understanding how these mechanisms occur in response to actual flow patterns in the molten steel is crucial to reducing defect formation. Most of these proposed mechanisms are more likely to occur during transient events, due to accompanying changes in the flow pattern. For example, shear instability, *i.e.* the Kelvin-Helmholtz instability, occurs when velocity along the slag/steel interface exceeds a critical value,[2] which could be caused by a sudden increase of steel flow rate in the nozzle due to severe stopper-rod/slide-gate movements.

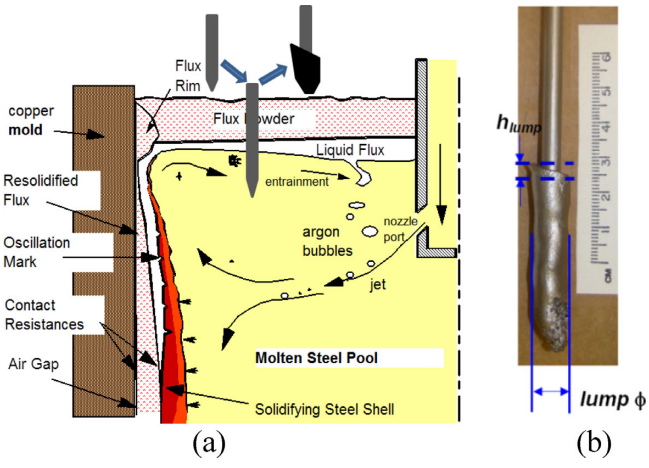

Fig. 1. Nail dipping procedure: (a) surface slag layers; (b) nail and lump. (Online version in color.)

* Corresponding author: E-mail: bgthomas@illinois.edu
DOI: http://dx.doi.org/10.2355/isijinternational.54.2314

Thus, understanding and avoiding defects require study of these transient events.

Several previous studies have investigated transient flow phenomena in the continuous casting mold region using computational models. Large Eddy Simulation (LES) has been applied to study transient flow during nominally steady-state flow conditions[5–9] including particle transport,[6] and the effect of electromagnetic forces.[8,9] However, genuine transient events and their corresponding large-scale flow variations have received less attention due to their complex nature. Huang and Thomas[10] developed a 3-D finite-difference model to simulate transient argon-steel two phase flow patterns in the mold, and found large scale vortex shedding phenomenon during the transition from asymmetric flow of nozzle clogging to steady symmetrical flow. Zhang *et al*. investigated flow during a cast startup process, utilizing a volume of fluid (VOF) model.[11] Few studies have attempted to measure flow in the mold during transient events.

In the current work, surface velocities in the mold during transient casting conditions were measured using two different sensors, which were validated with each other, and compared with predictions of a multi-phase computational model of the flow of argon and steel in the nozzle and mold, and includes two separate submodels to predict the flow rate. The validated model was then applied to simulate a transient flow event involving multiple stopper-rod movements.

2. Surface Velocity Measurement in Molten Steel Caster

Experimental methods are needed to monitor the real condition of flow in the mold, and to validate computational model predictions, especially for multiphase flow. Water models have frequently been utilized to for this purpose.[12,13] However, it has been found[14] that multi-phase flow behavior in air/water systems differs from that in argon/steel systems, due to surface tension, contact angle, and other differences. Similarly, oil/water systems are essentially different than molten-slag/steel systems. Moreover, the bottom of the water model and lack of a solidifying steel shell also changes the flow.[9,15] Thus, plant measurements are preferred over water models. The liquid steel surface velocity is a key indicator of flow problems: too high a surface velocity induces excessive turbulence and shear instability at slag-steel interface and increases the possibility of slag entrainment;[1] too low a surface velocity results in excessive cooling near the meniscus regions, which may further cause hook formation, nonuniform slag consumption, and the entrapment of mold slag, inclusion particles, or bubbles, leading to various surface defects.[16] Thus it is of great significance to find, validate, and apply methods to measure surface velocity in the mold.

2.1. SVC Sensor

Several different methods to measure liquid steel velocities have been developed and applied in previous work,[17–20] including Mass Flow Control (MFC) sensors,[17] Karman vortex probes,[18] and Sub-meniscus Velocity Control (SVC) sensors.[19] The SVC sensor involves dipping a rod into the molten steel and measuring the deflection angle and torque. These quantities are transformed into surface velocities, similar to the method of Kubota *et al*.[20]

2.2. Nailboard Method

A simple method to sample the slag layer and surface level conditions in the mold using nail boards was pioneered by Dauby *et al*.[21] at LTV Steel, then further developed by Thomas *et al*.[22–24] to measure surface velocity. In addition to measuring instantaneous surface steel velocities in the mold and the direction of flow, the nail board method can also provide the mold level (slag-steel interface) profile across the top surface, and the thickness profile of the slag layer.

For both nail board and single nail dipping tests, nails are inserted through the top-surface powder layers into the molten steel, held for 3–5 seconds, and removed. A lump forms on the bottom of each nail, due to the solidification of the liquid steel and slag, as shown in Figs. 1(a) and1(b). As molten steel flows past the nail, the liquid builds up at the impinging point on the nail lump before it solidifies. The kinetic energy of the impinging stream is converted into potential energy at the stagnation point as the impinging flow rises up the nail. The liquid-steel level drops at the opposite (downstream) side of the nail lump, due to the lower pressure in the wake region. This change in level of the slag-steel interface is recorded by the shape of the solidified lump, as shown in Fig. 1(b). By measuring the lump shape and lump height difference between the side facing the flow side and the opposite downstream side, the magnitude and direction of the surface steel velocity can be determined. A finite-element CFD model of the nail dipping test was developed by Rietow and Thomas[15,24] to study the liquid steel flow past a nail with a liquid slag layer on top. Their steady-state three-phase model tracked the two free surfaces, by deforming the mesh to maintain cell boundaries along the liquid slag/steel interface and the slag/powder interface. This model includes the effects of interfacial tension at the slag-steel interface (assuming 1.6 N/m) and predicts the interface shape and the height difference across the nail for a given bulk velocity of the steel beneath the interface.[15,24]

3. Plant Measurements

In the present work, three different plant trials were conducted in the No. 1 continuous caster at ArcelorMittal Dofasco, which has a 225 mm-thick mold with a bifurcated SEN with 15-deg downward ports. In trial #1, two different sensor techniques: the SVC device and single nail dipping tests, are used simultaneously, to independently measure the surface velocities during a time interval with many casting speed changes. The 25-mm diameter SVC probe was inserted 100 mm below the surface, midway between the SEN and narrow face, and instantaneous velocities were recorded at a sampling frequency of 1 Hz. A single nail with a diameter of ~5 mm was inserted about 50 mm closer to the narrow face than the SVC probe for each measurement. This location for dipping the nail was chosen so that the two sensing methods measured velocities at almost the same location at mold top surface, but also far enough apart so that the local flow around the nail did not disturb the SVC probe. The nail-dipping approach has since been used extensively to study the mold flow pattern in ArcelorMittal Dofasco.[25]

Next, trial #2 is a campaign of three heats cast under controlled conditions using only the validated nail-dipping

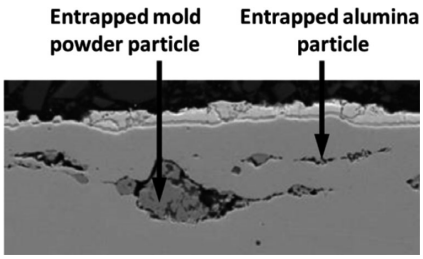

Fig. 2. SEM image of subsurface defects in trial #3.[26)]

Table 1. Processing parameters for plant trials.

Trial #	Mold Width (mm)	Mold Thickness (mm)	Casting Speed (m/min)	Sensing Methods	SEN Depth (mm)	Gas Injection Rat (SLPM)
1	1 248	225	1.0 – 1.9	SVC + Nail	177	6
2	983		1.5 – 1.9	Nail	185	
3	1 472		1.2	Eddy Current	166	

method to quantify liquid steel surface velocities, in order to validate the multi-phase CFD model. Casting speed is varied with the same argon flow rate in order to quantify how gas fraction changes the flow pattern, which can be determined experimentally by recording the changing direction and magnitude of the surface flow velocity.

Finally, Trial #3 is a transient event with carefully recorded time-histories of the stopper-rod position, the mold level measured using an eddy current sensor at mold quarter point, the casting speed, and argon gas flow rate. Sliver defects were detected on coils with the aid of downstream feedback from the Automated Surface Intelligence System™ (ASIS™).[26)] An SEM image of the defects obtained from the coil sample chosen for this study are pictured in **Fig. 2**. Their compositions indicate entrapped mold flux and alumina particles. Next, the locations of defects formation on slabs were calculated from the entrapment depths in the coil, knowing the defects locations along the coil length and the thickness reduction ratios between the coils and slabs. This particular defect corresponds to a shell thickness of 3.2 mm in the 218 mm-thick slab. This suggests that the defect chosen in this work was formed by the entrapment of inclusion particles in the mold, about 27 mm below the meniscus. The time of particle entrapment was calculated from the recorded casting speed and cast length data, which defines the transient event of trial #3. The process conditions and sensing methods used in measurements for all three trials are listed in **Table 1**.

4. Validation and Calibration of Nail Dipping Method

To interpret the nail-board measurements, a new equation to quantify the liquid steel surface velocity is given by Eq. (1) based on the results from the previous computational modeling studies from Rietow and Thomas,[24)] which are included in **Fig. 3**. Equation (1) correlates the average liquid steel velocity magnitude just below the slag/steel interface with the difference in height of opposite sides of the solidified lump and with the lump diameter.

$$V_s = 0.624\phi_{lump}^{-0.696} h_{lump}^{0.567} \quad \text{..... (1)}$$

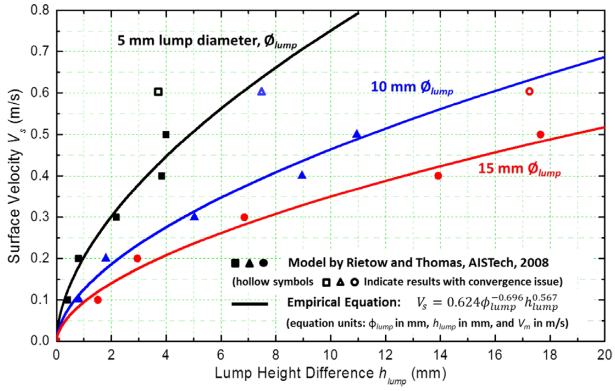

Fig. 3. Curves to convert nail lump height difference into velocity magnitude at the top surface. (Online version in color.)

where V_s is steel surface velocity (m/s), ϕ_{lump} is lump diameter (mm), and h_{lump} is lump height difference (mm). It is worth pointing out that the previous results by Rietow[24)] predict a maximum lump height difference, which was less than observed for lumps at high surface velocity in the current work. This suggests that Rietow's simulation results at the highest surface velocity of 0.6 m/s likely had convergence problems causing numerical error. Thus, those results (shown as hollow symbols) were excluded from the least square regression process that generated the new Eq. (1).

In trial #1, casting speed was varied greatly as shown in **Fig. 4**(a) and the corresponding steel surface velocity histories monitored by both SVC and nail dipping are shown in Fig. 4(b). Casting conditions noted in Table 1 include argon gas injection into the upper tundish nozzle (UN), stopper rod (SR), and SEN at a total rate of 6 SLPM. In addition to the instantaneous SVC surface velocity measured, Fig. 4(b) also shows a 30-second moving average velocity. Positive surface velocities indicate flow towards the SEN, and negative velocities indicate flow towards the narrow face. The locations where the nail and SVC probe were inserted are also given in Fig. 4(b). Error bars for the nail dipping test results were obtained assuming an uncertainty of 0.5 mm in measuring both the lump diameter and the lump height difference.

The SVC data and nail dipping results match closely with each other, as shown in Fig. 4(b). Furthermore, most nail dipping measurements match the moving average of the SVC data. At a few points, the nail dipping results fall outside the moving average, but still always fall within the range of the instantaneous SVC data. Perhaps the velocities from the nail dipping measurements are slightly less than the SVC data. This might be expected, considering that the SVC probe extends to 100 mm below the surface and measures an average over that range. The nail dipping test measures velocity closer to the surface, which should be lower, owing to the viscous drag effect from the slag layer.

5. Computational Model Description

A model system has been developed to simulate multiphase flow evolution during transient events with actuator movements. It consists of 1) a stopper-position-based model, or a metal-level-based model to predict liquid steel flow rate inside SEN during stopper rod movements which is required as a boundary condition for the two-phase flow

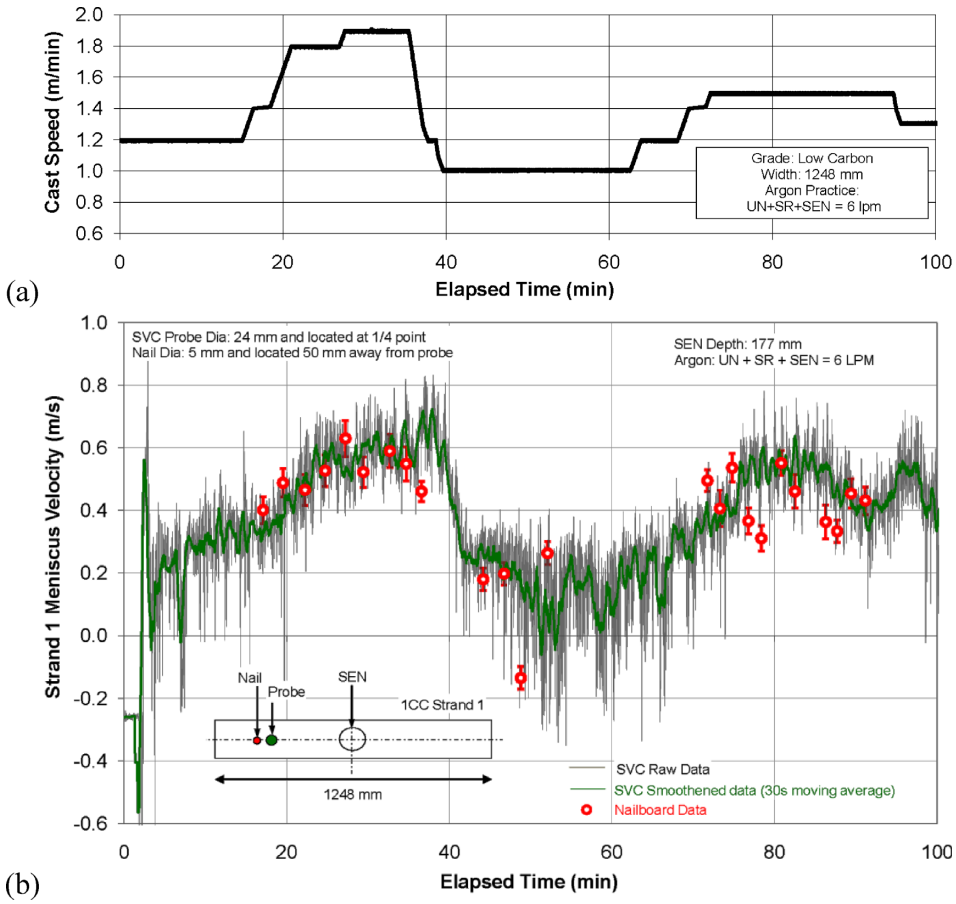

Fig. 4. Casting speed change in trial #1 and measured surface velocity: (a) casting speed change ; (b) surface velocity history from SVC and nail dipping.[35] (Online version in color.)

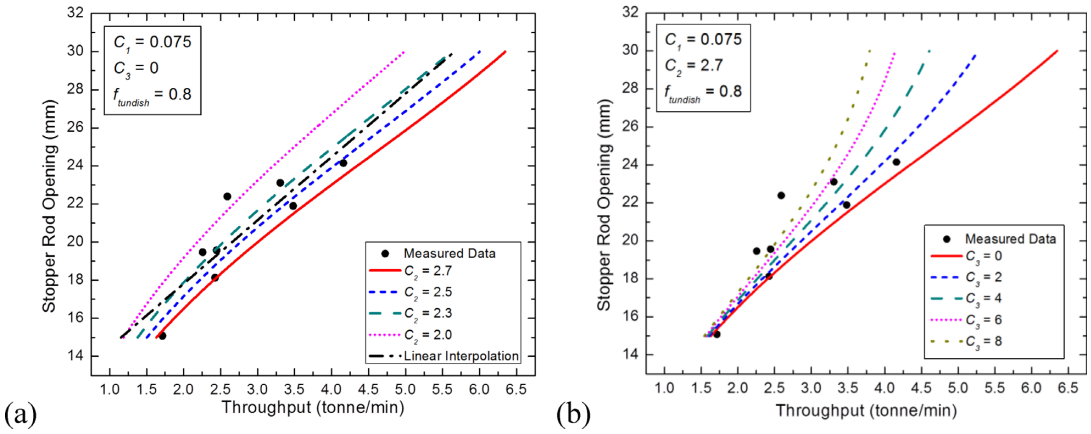

Fig. 5. Effects of C_2 and C_3 on stopper-position-based model predictions of flow rate. (Online version in color.)

simulations;[27] 2) a porous gas flow model to estimate hot argon flow rate into the liquid steel stream in the nozzle, and the resultant mean bubble size entering the nozzle, as explained elsewhere;[28] and 3) an Eulerian-Mixture CFD model to simulate argon-steel two-phase flow in the nozzle and mold region, and a pressure-based post-processing method to estimate meniscus level. These models are summarized briefly in the following 3 sections. Further details are reported elsewhere.[27,28]

5.1. Stopper-position-based Model of SEN Steel Flow Rate

During steady-state continuous casting, the liquid steel flow rate into the SEN equals the throughput at mold exit. During a transient event, however, steel flow rate in the SEN varies with time, as indicated by the rapid fluctuations of the average mold level. Two different models were developed in this work to predict the liquid steel flow rate in the SEN.

Firstly, a semi-analytical model, given in Eq. (2), is derived from Bernoulli's equation to predict flow rate based on the measured stopper rod opening position and other parameters, with the details of the derivation found elsewhere.[27,29] It is validated with plant measurements, as shown in **Fig. 5**.

$$Q_{SEN} = A_{SEN}\left(\frac{2g\left(f_{tundish}h_{tundish} - h_{sen\_sub} + L_{SEN}\right)}{1+0.5\left(\frac{A_{SEN}}{C_2h_{SRO}^2}\right)^2+\left(\frac{A_{SEN}}{C_2h_{SRO}^2}-1\right)^2+C_1\frac{L_{SEN}}{D_{SEN}}+C_3}\right)^{0.5} \quad \text{..... (2)}$$

In this equation, A_{SEN} is the SEN inner bore cross-section area; h_{sen_sub} is the submergence depth of SEN, $f_{tundish}$ is the tundish weight fraction, typically measured to be 80%, relative to 100% full at the total height of the tundish, $h_{tundish}$, (1.45 m); L_{SEN} is the total length of the SEN (1.1 m); D_{SEN} is the SEN inner bore diameter (75 mm); h_{SRO} is the measured stopper rod opening. The three adjustable coefficients represent different pressure head losses: C_1 for friction, C_2 for the stopper rod gap and C_3 for clogging. Here, C_1 is 0.075 from the Moody chart,[29] but the effect of friction factor on the predicted relation is negligible. The influence of C_2 and C_3 is shown in Fig. 5. The effect of argon gas injection on the pressure head loss at the stopper rod gap is accounted for in C_2. Here, C_2 was calibrated to be 2.7 using the plant trial data in Fig. 5(a), which had the same gas volume fraction as in the current transient study (10% gas). In this work, clogging was ignored, so C_3 is 0.

5.2. Metal-level-based Model of SEN Steel Flow Rate

A metal-level-based model was also derived to predict steel flow rate, based on an overall mass conservation of the system. Knowing the casting speed, the time variation of the liquid steel flow rate in the SEN can be predicted from the mold level and casting speed histories recorded in the plant as follows:

$$Q_{SEN} = \frac{dh_l}{dt}\left(WS - \frac{\pi}{4}D_o^2\right) + V_{cast}WS \quad \text{..... (3)}$$

In this equation, t represents time; V_{cast} is the casting speed; W is the mold width, S is the mold thickness; h_l is the average mold level; and D_o is the SEN outer bore diameter (130 mm). A central-difference time-discretization of the mold level position history is used to calculate dh_l/dt, based on the eddy-current level sensor measurements midway across the mold,[27] which are assumed to be representative of the average liquid level in the mold. This model was used as validation for the predictions from the entire model system, including the stopper-position-based flow rate model.

5.3. Model of Gas Flow Rate and Initial Bubble Size in Nozzle

Because gas expands at high temperature, the hot argon flow rate will be ~4 to 5 times higher in the mold than measured at room temperature (STP). The size of the resulting argon bubbles depends on gas flow through the porous nozzle refractory and significantly affects steel flow in the mold. A new 3-D porous-flow model[28] was developed and used to calculate argon gas velocity distribution inside the upper tundish nozzle and exiting the inner surface, taking into account the effects of gas thermal expansion, nozzle geometry, temperature-dependent gas viscosity, and interfacial tension forces at the gas pores. After solving for the temperature distribution inside the nozzle, Eq. (4) was solved to obtain the pressure distribution in the refractory,

$$\nabla\cdot\left(K_D\nabla p\right) = -\frac{RT}{p}\left[\nabla\left(\frac{p}{RT}\right)\cdot\left(K_D\nabla p\right)\right] \quad \text{..... (4)}$$

where T is the local temperature in refractory, p is gas pressure, R is the gas constant and K_D is the permeability. Then the gas velocities were calculated from the pressure field following Darcy's law. The results are combined with an empirical equation to estimate active sites number density from Lee *et al*.[30] and a semi-empirical two-stage bubble formation model from Bai and Thomas[31] to predict initial bubble size entering the SEN. A mean bubble diameter of 2.5 mm was obtained for this work. Details on the gas porous-flow model and calculation of the initial bubble size are given elsewhere.[28,30,31]

5.4. Multiphase Fluid Flow Model

Argon-steel two-phase flow in the nozzle and mold was simulated with a transient 3-D Eulerian-Mixture model, which satisfies mass and momentum conservation of the argon-steel mixture by solving the continuity Eqs. (5) and (6), and one set of Unsteady Reynolds-Averaged Navier Stokes (U-RANS) Eq. (7):

$$\frac{\partial\rho_m}{\partial t} + \nabla\cdot\left(\rho_m\mathbf{u}_m\right) = 0 \quad \text{..... (5)}$$

$$\text{where } \mathbf{u}_m = \frac{\alpha_s\rho_s\mathbf{u}_s + \alpha_a\rho_a\mathbf{u}_a}{\rho_m}, \text{ and } \rho_m = \alpha_s\rho_s + \alpha_a\rho_a \quad \text{... (6)}$$

$$\rho_m\left(\frac{\partial\mathbf{u}_m}{\partial t} + \left(\mathbf{u}_m\cdot\nabla\right)\mathbf{u}_m\right) = -\nabla p + \nabla\cdot\left[\mu_m\left(\nabla\mathbf{u}_m + \left(\nabla\mathbf{u}_m\right)^T\right)\right] + \rho_m\mathbf{g} + \nabla\cdot\left(\alpha_a\rho_a\mathbf{u}_{dr,a}\mathbf{u}_{dr,a}\right) \quad \text{..... (7)}$$

where ρ is density, α is volumetric phase fraction, and the subscripts a, s, and m represent argon, steel, and multiphase mixture respectively. The phase fractions are found by solving Eq. (8), and knowing that α_a and α_s sum to 1.

$$\frac{\partial\left(\alpha_a\rho_a\right)}{\partial t} + \nabla\cdot\left(\alpha_a\rho_a\mathbf{u}_m\right) = -\nabla\cdot\left(\alpha_a\rho_a\mathbf{u}_{dr,a}\right) \quad \text{..... (8)}$$

Drift velocity $\mathbf{u}_{dr,a}$ on the right hand side of Eqs. (7) and (8) is defined in Eq. (9).

$$\mathbf{u}_{dr,a} = \mathbf{u}_{as} - \frac{\alpha_a\rho_a}{\rho_m}\mathbf{u}_{as}, \text{ where the relative velocity is}$$
$$\mathbf{u}_{as} = \mathbf{u}_a - \mathbf{u}_s \quad \text{.... (9)}$$

The mixture model is then closed using an algebraic slip formulation for the relative velocity $\mathbf{u}_{as}$ assuming that local equilibrium between phases is reached over a short spatial length, as given in Eq. (10),[32] where the drag function f_{drag} is taken from Schiller and Naumann[33] and d_a is the argon bubble diameter (2.5 mm), calculated as discussed in Section 5.2,

$$\mathbf{u}_{as} = \frac{\left(\rho_a - \rho_m\right)d_a^2}{18\mu_s f_{drag}}\left(\mathbf{g} - \left(\mathbf{u}_m\cdot\nabla\right)\mathbf{u}_m - \frac{\partial\mathbf{u}_m}{\partial t}\right) \quad \text{.... (10)}$$

The standard k-ε model was applied to model turbulence in the mixture phase.

The computational domain includes the nozzle and the liquid pool in the mold region, with the solidification front interface as the domain boundary. No-slip wall boundary condition is adopted both at the shell boundary and at the mold top surface, as the sintered slag layer serves as a solid wall, with an enhanced wall treatment (EWT)[34] to calculate near-wall velocities. Mass and momentum sinks are imposed at the layer of computational cells next to the shell boundary, to account for the liquid steel crossing the boundary due to solidification. Similar mass and momentum sinks are applied to quantify the argon gas escaping from the top surface. For the steady-state simulations in trial #2, one quarter of the nozzle and mold were chosen as the computational domain with a mesh of ~0.23 million hexahedral cells. For the transient simulation of 30 s of trial #3, the entire-mold domain was modelled with a mesh of 0.8 million mapped hexahedral cells as shown in **Fig. 6**, and time step size was 0.01 sec.

6. Investigation of Casting Condition Effects on Surface Velocity

The trial #1 and #2 plant measurements of surface velocity and the model simulations reveal insights into the critical combined effects of gas injection, casting speed and mold width on the flow pattern in the mold. Although argon gas flow rate remains constant, the gas volume fraction varies with throughput according to changes in casting speed and width. **Figure 7** shows the measured nail surface velocity points and SVC data samples over 1s-intervals for 3 heats of steel at each mold width (1 248 mm in trial #1 and 983 mm in trial #2).[35] The gas volume fraction is presented in the hot condition, which is ~4–5 times larger than measured at STP, as explained in Section 5.3. Steady-state CFD simulations were also performed for three casting speeds (1.5, 1.7, and 1.9 m/min) at the same argon flow rate (6 SLPM) of trial #2 to reveal the flow patterns, which are presented in **Fig. 8**.

6.1. Model Validation

The calculated surface velocities are compared with results of the plant nail dipping tests in **Fig. 9**, in which symbols are the mean velocities from the ten nail samples for each casting speed in trial #2, and error bars indicate the standard deviation. As shown in Fig. 9,[27] a reasonable match is obtained between the simulated surface velocities and those from nail-dipping tests, which tends to validate the model.

6.2. Effect of Casting Speed

For both mold widths and a fixed gas injection flow rate (6 SLPM), Fig. 7[35] shows that liquid steel surface velocity increases with casting speed. For a constant mold width and gas injection rate, higher casting speed has two effects: increasing mean velocity of the liquid steel at the SEN port exit and lowering the gas volume fraction. Both effects encourage higher surface velocities. The simulated liquid steel flow patterns in Fig. 8 are generally double-roll flow

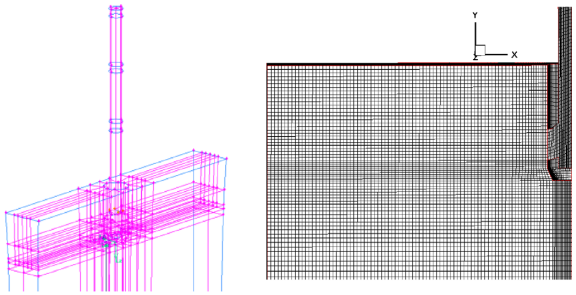

Fig. 6. Computational domain for full mold simulation: (a) geometry and (b) cutaway view of mesh. (Online version in color.)

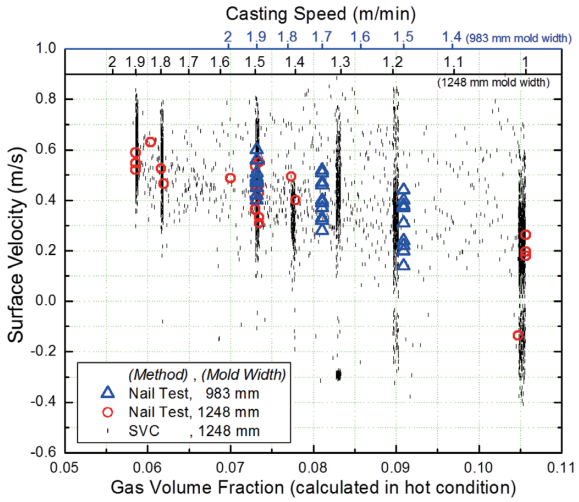

Fig. 7. Effects of casting speed, mold width and gas volume fraction (in hot condition) on surface velocity (trials #1 and #2).

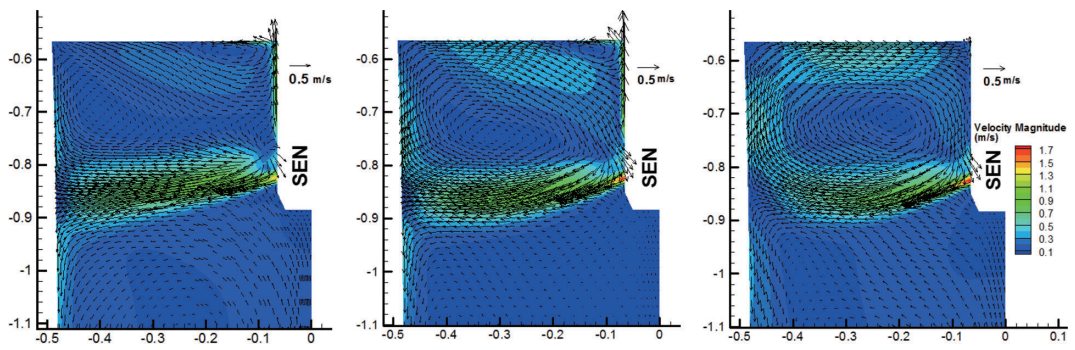

(a) 1.5 m/min; (b) 1.7 m/min (c) 1.9 m/min

Fig. 8. Flow patterns with different argon gas volume fractions, with varying casting speeds.

patterns, especially at high casting speed (Fig. 8(c)). In Fig. 8(a) (1.5 m/min), however, some gas rises from the SEN port exit, drags steel upward, and causes liquid surface flow away from the SEN. This could be termed a complex flow pattern, tending towards a single-roll flow pattern. A small recirculation region is found near the surface near the SEN. Figure 8(b) shows that increasing casting speed (1.7 m/min) decreases the size of this recirculation region. The reverse velocity away from the SEN also decreases, as shown in Fig. 9 while on the rest of the surface, the velocity towards the SEN increases. Increasing speed to 1.9 m/min causes the recirculation region near the SEN to disappear. Surface velocity towards the SEN further increases and the effects of gas injection become negligible. It is also observed that for higher casting speeds, the vortex center of the upper roll moves closer to SEN.

Casting speed also has a great effect on the variability of the surface velocity. Figure 7 shows that increasing casting speed decreases the incidence of instantaneous reverse flow at the measured points midway across the mold, especially in the SVC data. This indicates increasing tendency towards a stable double-roll flow pattern. This suggests more stable flow in the mold for higher casting speeds with double-roll flow patterns.

6.3. Effect of Mold Width

Figure 7 has results at two different mold widths. At the same casting speed, surface velocities in the narrow (983 mm) mold are lower than in the wide (1 248 mm) mold (both SVC and nail dipping). Increasing mold width causes higher throughput, which increases steel velocity exiting the SEN ports. This increase in SEN velocity is offset slightly by the increased distance for the jet to travel from SEN port exit to meniscus, which diffuses the jet momentum more. The net effect is that surface velocity is still higher in the wider mold (1 248 mm) at the same casting speed. The measurements in Fig. 7 also suggest that this effect of mold width becomes less significant at higher casting speeds (*e.g.* 1.9 m/min).

Increasing mold width also appears to have increasing flow stability, as the surface velocity variations are smaller for the larger width at the same speed. However, this might be caused by the change in gas fraction. It is important to mention that this finding is based on relatively narrow mold widths (1 248 and 983 mm). For much wider molds (*e.g.* 1 800 mm or wider), other work[36] suggests that flow pattern and surface velocity variations increase due to increased large-scale jet instability.

6.4. Effect of Gas Volume Fraction

Gas fraction changes with both casting speed and mold width, so has an important influence to explain the trends presented in the previous 2 sections. Figure 7 shows that the measured surface velocities at mold quarter point decrease almost linearly with increasing gas volume fraction. All three sets of measurements from both trials consistently show that increasing gas volume fraction causes a transition of flow pattern from double-roll to complex flow, especially as the gas volume fraction approaches ~10%.

Simulation results in Fig. 8 confirm and explain this observation that increasing gas volume fraction (by decreasing casting speed), tends to change the double-roll flow pattern into a complex flow pattern. Argon bubbles are carried by the liquid steel jet into the mold, and then float up to the top surface and exit the domain, as suggested by the quasi-steady gas volume fraction distribution for trial #3 presented in **Fig. 10**. The buoyant gas bubbles rising near the SEN oppose the surface flow towards the SEN from the narrow face. This reverse flow alters the double-roll flow pattern towards a complex or even single-roll flow pattern, and causes the observed drop in surface velocity with increasing gas fraction.

7. Transient Event Simulation Results

The system of models is next applied to simulate the transient event of trial #3 involving multiple large stopper-rod movements, that is described in Section 2 and Table 1. The stopper-rod position, mold level and casting speed histories recorded in the plant database during this event are shown in **Fig. 11**. The time when the sliver defect in Fig. 2 was formed is also shown. A transient two-phase flow simulation was performed with the Eulerian-Mixture model, based on the stopper-position-based flow rate, after initializing with a solution at steady-state conditions (gas distribution shown in Fig. 10).

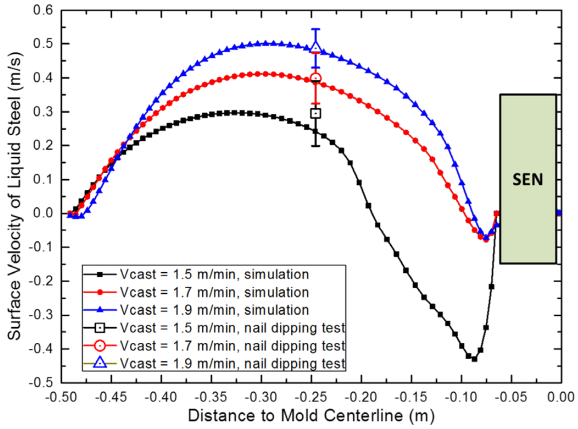

Fig. 9. Comparison between predicted and measured surface velocities from trial #2. (Online version in color.)

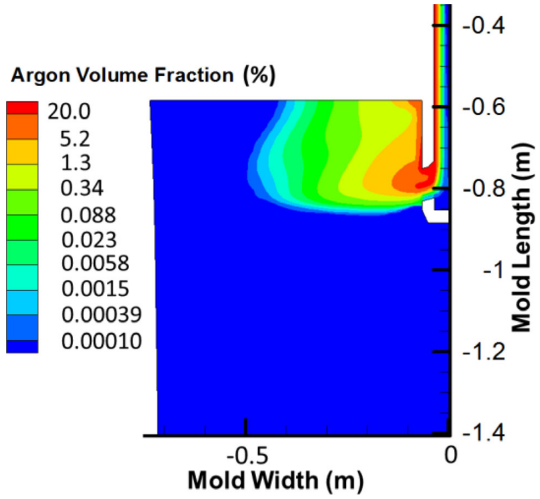

Fig. 10. Quasi-steady state argon volume fraction distribution (trial #3). (Online version in color.)

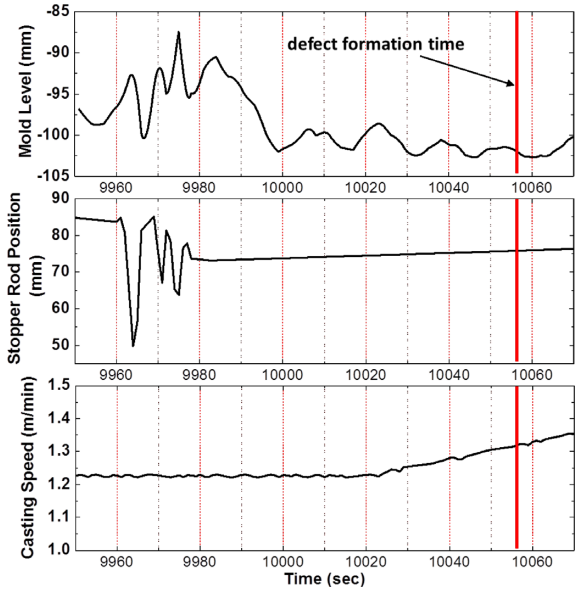

Fig. 11. Recorded stopper rod position, mold level and casting speed (trial #3).[27] (Online version in color.)

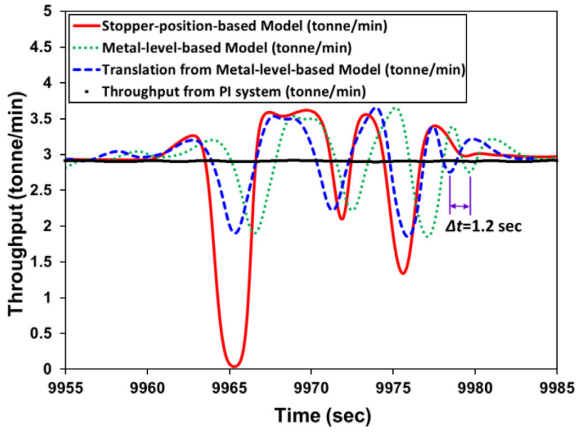

Fig. 12. Predicted SEN flow rates from stopper-position-based and metal-level-based model (for trial #3). (Online version in color.)

7.1. SEN Inlet Liquid Steel Flow Rate History

The liquid steel flow rate in the SEN predicted by the stopper-position-based model and the metal-level-based model are compared in **Fig. 12**. Note that translating the metal-level-based results back in time by about 1.2 sec (dashed line in Fig. 12) makes the two predicted curves roughly match. This time delay is likely related to traveling waves on the mold top surface. The average mold level based on the SEN position responds instantly to flow rate changes. Flow disturbances travel across the top surface, and the measured level signal at the mold quarter point records it later. Therefore, the SEN flow rate from the stopper-position-based model is adopted for the inlet boundary condition in the transient simulation. The simulation investigates flow pattern evolution from 9 955 to 9 985 sec, (30.0 sec), which includes a major flow-rate drop around 9 965 sec due to declogging, by bumping of the stopper rod in an attempt to dislodge the buildup of inclusions on the stopper tip.

7.2. Flow Pattern Evolution

Evolution of the flow pattern in the mold simulated during the first 16.7 sec of trial #3 is shown in **Fig. 13**.[37] Each frame is plotted at the center plane between mold broad faces. The initial quasi-steady state flow field (at 9 955 sec), is observed to be a symmetric double-roll flow pattern, which is expected for these conditions (9.6% gas).

As the inlet liquid steel flow rate decreases, (*e.g.* at 9 964 sec), the strength of the jets decrease. Jet strength continues to decrease (9 965.7 sec) and then starts to recover (at 9 966.3 sec). Then, (at 9 967.2 sec), a strong burst of liquid steel shoots up towards the meniscus near the SEN, and significant disturbance of the meniscus is observed. This likely causes liquid slag droplets to become entrained into the liquid pool. This phenomenon is probably caused by the strong buoyancy force from a large amount of rising argon gas accumulated in the nozzle during the stopper-rod closing stage. Between time 9 968 and 9 969.1 sec, the upward liquid stream towards meniscus becomes less intensive, and liquid steel jets towards the narrow faces begin to develop, and wobbling of the jets is observed. Finally, at time 9 971.7 sec, the jet swinging disappears, and the symmetrical quasi-steady flow pattern becomes re-established.

7.3. Comparison of Predicted and Measured Mold Level

The flow pattern changes caused by the stopper rod movements also affect the mold level profile and cause fluctuations of the top surface level, which can be detrimental to steel quality. In this simulation, the top surface cannot move as a wall boundary so the local mold level is predicted from a simple energy balance, converting the pressure difference into the potential energy of the level elevation head by Eq. (11):

$$\Delta h = \frac{p - p_0}{\rho_s g} \quad \text{.....(11)}$$

where Δh is the mold level deviation, p is pressure along the top surface, and p_0 is the pressure at the reference mold level, which is taken at the mold quarter point from steady-state solution. ρ_s is the liquid steel density (7 200 kg/m^3), and g is gravitational acceleration (9.81 m/s). Displacement of the liquid slag layer is neglected in this equation, because the entire layer was assumed to be thin enough to simply rise and fall with the steel surface profile variations. This assumption agrees with recent measurements by Cho *et al*.[38]

The predicted mold level during the simulated 30.0 sec interval with stopper rod movements agrees reasonably well with the measured unfiltered mold level data, at the midway point between SEN and narrow face along the centerline, as shown in **Fig. 14**. However, the measured mold level signal is delayed by about 2 sec.[37] This discrepancy is explained by the inability of the simple pressure method to capture transient waves or gravity wave sloshing, since the pressure method forces an immediate response to flow rate changes. The measured response delay consists of two parts: the time needed for the average free surface level to respond to the flow rate change, and the time for the surface wave to travel to the location of measurement (around quarter mold point). Note also that there is significant asymmetry between the left and right sides of the mold, owing to chaotic turbulence.

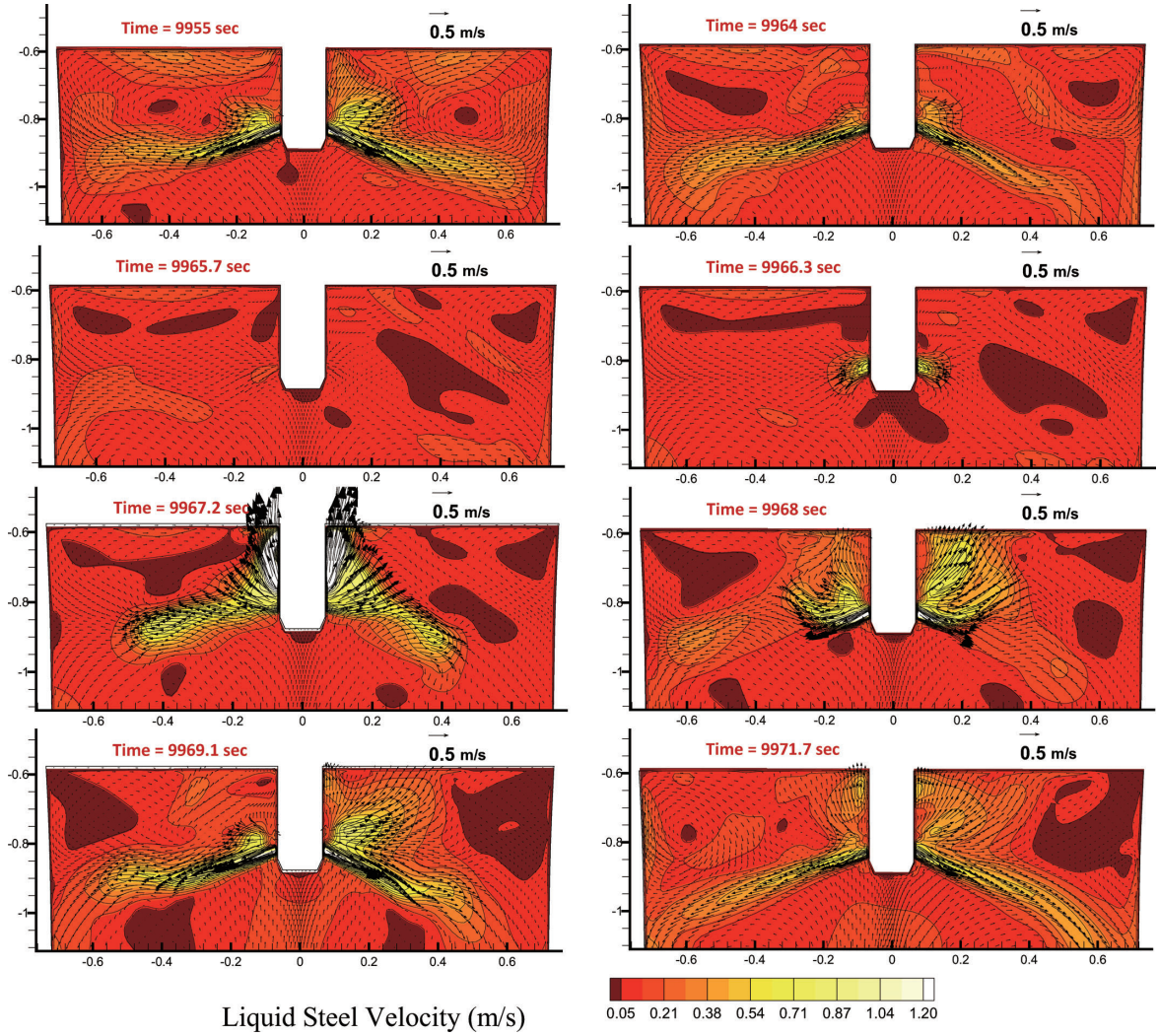

Fig. 13. Transient flow patterns during stopper rod movement in trial #3 (axis distances in m).

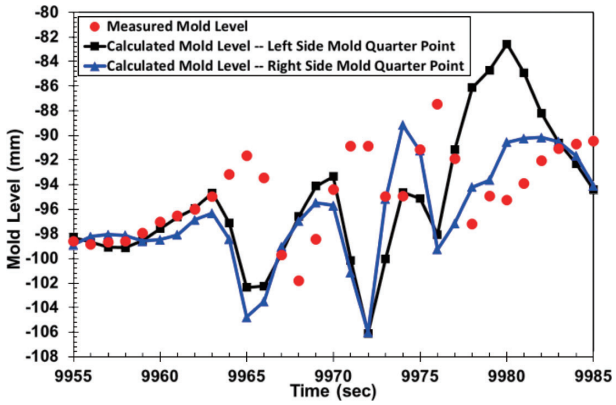

Fig. 14. Comparison of calculated and measured mold level (for trail #3).

7.4. Defect Formation Mechanisms

The sliver defects in the final product produced just after this transient event are related to the evolution of the two-phase flow field. The simulations show that the multiple stopper-rod movements clearly induced flow changes in the mold and level fluctuations. Different mechanisms could explain exactly how this occurred. One possible cause is that the sudden large mold level changes immediately entrapped slag particles into the solidifying shell at the meniscus. In this case, however, ~60 sec passed after the mold level disturbances before the particle was entrapped. The stopper movements likely dislodged a build-up of clog material inside the SEN, releasing inclusion particles into the mold. In addition, the surface flow variations may have entrained mold slag droplets into the steel flow in the mold. These particles then circulated in the transient mold flow for some time before eventually becoming entrapped into the solidification front, leading to slivers in the rolled product.

As a consequence of this investigation into the mechanism of defect formation, this method for declogging has been abandoned in ArcelorMittal Dofasco. Instead, a stopper-rod dithering approach has been adopted as a standard practice to reduce clogging, without significantly disturbing the molten steel surface in the mold, and has shown satisfying performance.[39]

8. Conclusions

Three plant trials were carried out to investigate the effect of casting conditions on fluid flow in a conventional steel slab caster mold and the cause of coil defects. A system of computational models was developed, validated with the measurements, and implemented to study both steady and transient multi-phase flow in these trials. The following con-

clusions are drawn:

(1) A new correlation to quantify steel surface velocity from nail dipping plant tests, based on solidified lump height difference, and lump diameter.

(2) An SVC system can provide reliable continuous surface velocity measurements in molten steel and successfully validated the nail dipping tests in the current work.

(3) Nail dipping is a simple, reliable, and capable method to simultaneously measure instantaneous top surface steel velocities and flow directions at multiple locations, in addition to slag layer thickness and surface level profiles.

(4) Flow rate models, including a stopper-position-based model, have been developed, validated and used to predict the time-dependent flow rates of steel in the nozzle, which is required to provide accurate inlet conditions for transient simulations.

(5) Surface velocity increases with increasing casting speed and/or decreasing gas volume fraction, as the flow pattern tends towards double-roll. With high gas fractions, such as caused by low casting speed, surface velocity decreases and flow reversals (flow directed away from the SEN) are more often observed.

(6) The flow pattern becomes more complex and continuously changing with increasing gas fraction, as the reverse surface flow away from the SEN is predicted to meet flow from the narrow face. The meeting point changes with time, causing flow reversals to be recorded at the mid-point sensor with increasing likelihood as the gas fraction increases.

(7) The effect of increasing mold width is complicated because it increases port velocity, increases travel distance, and increases throughput, which decreases gas fraction, with a net effect of increasing surface velocity and tendency towards double-roll flow in the current study.

(8) Transient flow events, such as due to excessive stopper rod movements, cause significant disturbances of the meniscus and transient mold flow, which may entrain slag, leading later to particle entrapment into the solidifying shell and the sliver defects in the final product.

(9) The model system predictions agree reasonably well with the plant measurements. This system is a useful tool to study transient flow phenomena, especially when combined with plant measurements.

Acknowledgements

This work was supported by the Continuous Casting Consortium at the University of Illinois. The authors are also grateful to ArcelorMittal for providing support and plant data for this project, and to other personnel including D. Crosbie and D. Currey at ArcelorMittal Dofasco Global R&D in Canada, and M. Yavuz at ArcelorMittal Global R&D in East Chicago for their help with the experimental work. ArcelorMittal Global R&D in Maizières, France is acknowledged for providing the SVC devices for trials.

REFERENCES

1) T. Watanabe and M. Iguchi: *ISIJ Int.*, **49** (2009), 182.
2) J. Hartman and A. Cramb: Proc. of Steelmaking Conf., ISS, Warrendale, PA, (1996), 773.
3) L. C. Hibbeler and B. G. Thomas: Proc. of AISTech 2013 Steelmaking Conf., AIST, Warrendale, PA, (2013), 1215.
4) B. G. Thomas: Making, Shaping and Treating of Steel, Chapter 14, Casting Volume, 11th ed., ed. by A. Cramb, AISE Steel Foundation, Pittsburgh, PA, (2003), 1.
5) Q. Yuan, B. G. Thomas and S. P. Vanka: *Metall. Mater. Trans. B*, **35B** (2004), 685.
6) B. G. Thomas, Q. Yuan, S. Mahmood, R. Liu and R. Chaudhary: *Metall. Mater. Trans. B*, **45B** (2014), 22.
7) R. Liu, W. Ji, J. Li, H. F. Shen and B. C. Liu: *Steel Res. Int.*, **79** (2008), 50.
8) R. Chaudhary, C. Ji, S. P. Vanka and B. G. Thomas: *Metall. Mater. Trans. B*, **42** (2011), 987.
9) R. Singh, B. G. Thomas and S. P. Vanka: *Metall. Mater. Trans. B*, **44** (2013), 1201.
10) X. Huang and B. G. Thomas: *Can. Metall. Q.*, **37** (1998), 197.
11) Y. Wang and L. Zhang: *ISIJ Int.*, **50** (2010), 1777.
12) B. G. Thomas, X. Huang and R. C. Sussman: *Metall. Mater. Trans. B*, **25B** (1994), 527.
13) Z. Wang, K. Mukai, Z. Ma, M. Nishi, H. Tsukamoto and F. Shi: *ISIJ Int.*, **39** (1999), 795.
14) R. C. Sussman, M. T. Burns, X. Huang and B. G. Thomas: 10th Process Tech. Conf. Proc., ISS, Warrendale, PA, (1992), 291.
15) B. Rietow: Master's Thesis, University of Illinois at Urbana-Champaign, (2007).
16) J. Sengupta, H. J. Shin, B. G. Thomas and S. H. Kim: *Acta Mater.*, **54** (2006), 1165.
17) K. U. Kohler, P. Andrzejewski, E. Julius and H. Haubrich: Proc. of Steelmaking Conf., ISS, Warrendale, PA, (1995), 445.
18) M. Iguchi and Y. Terauchi: *ISIJ Int.*, **42** (2002), 939.
19) J.-F. Domgin, P. Gardin, J.-M. Galpin and A. Dez: *Rev. Metall. -CIT*, **102** (2005), No.10, 703.
20) J. Kubota, N. Kubo, T. Ishii, M. Suzuki, N. Aramaki and R. Nishimachi: *NKK Tech. Rev.*, **85** (2001), 1.
21) P. H. Dauby, W. H. Emling, and R. Sobolewski: *Ironmaker Steelmaker*, **13** (1986), 28.
22) R. McDavid and B. G. Thomas: *Metall. Mater. Trans. B*, **27B** (1996), 672.
23) K. Cukierski and B. G. Thomas: *Metall. Mater. Trans. B*, **39B** (2007), 94.
24) B. Rietow and B. G. Thomas: Proc. of AISTech 2008 Steelmaking Conf., Warrendale, PA, (2008), 75.
25) J. Sengupta, D. Crosbie, S. Chung, M. Trinh, E. Dillon, J. Dixon, V. Gueugnon and J. Domgin: Proc. of AISTech 2011 Steelmaking Conf., AIST, Warrendale, PA, (2011), 1697.
26) E. M. Dillon, M. Sohm and D. Peters: Proc. of AISTech Steelmaking Conf., Warrendale, PA, (2008), 523.
27) R. Liu, J. Sengupta, D. Crosbie, M. M. Yavuz and B. G. Thomas: Proc. of AISTech Steelmaking Conf., Warrendale, PA, (2011), 1619.
28) R. Liu and B. G. Thomas: Proc. of AISTech Steelmaking Conf., Warrendale, PA, (2012), 2235.
29) F. M. White: Fluid Mechanics, 5th ed., McGraw-Hill, New York, (2003), 366.
30) G. Lee, B. G. Thomas and S. Kim: *Metall. Mater. Int.*, **16** (2010), 501.
31) H. Bai and B. G. Thomas: *Metall. Mater. Trans. B.*, **32B** (2001), 1143.
32) ANSYS Inc: FLUENT 6.3-Manual, Lebanon, NH, (2007).
33) L. Schiller and Z. Naumann: *Z. Ver. Deutsch. Ing.*, **77** (1935), 318.
34) U. Goldberg, O. Peroomian and S. Chakravarthy: *J. Fluid. Eng.*, **120** (1998), 457.
35) R. Liu, J. Sengupta, D. Crosbie, S. Chung, M. Trinh and B. G. Thomas: TMS Annual Meeting, TMS, Warrendale, PA, (2011), 51.
36) M. Brummayer, P. Gittler and J. Watzinger: 8th VAI Continuous Casting Conf. Proc., Linz, (2000), 81.
37) R. Liu, B. G. Thomas and J. Sengupta: Modeling of Casting, Welding, and Advanced Solidification Processes (MCWASP) XIII, Styria, (2012).
38) S. Cho, S. Kim and B. G. Thomas: *ISIJ Int.*, **54** (2014), 845.
39) S. D. Chung, J. Sengupta and M. Afnan: Proc. of AISTech 2013 Steelmaking Conf., Warrendale, PA, (2013), 1557.